





Cite this: *Nanoscale Adv.*, 2023, 5, 412

Early stages of polycrystalline diamond deposition: laser reflectance at substrates with growing nanodiamonds†

David Vázquez-Cortés,  Stoffel D. Janssens,  Burhannudin Sutisna 
and Eliot Fried *

The chemical vapor deposition of polycrystalline diamond (PCD) films is typically done on substrates seeded with diamond nanoparticles. Specular laser reflectance has been used in tandem with a continuous film model to monitor the thickness of these films during their deposition. However, approaches to gain information on properties that strongly affect film morphology, such as the areal density of seeds, remain largely unexplored. This work outlines a strategy for using laser reflectance measurements to refine the monitoring of film thickness during deposition, estimate the mean equivalent radii and the areal density of seeds, and estimate growth incubation periods. We present a general model based on the Rayleigh theory of scattering for laser reflectance at substrates with growing nanoparticles that captures the early stages of PCD deposition. We test our model experimentally by depositing diamond under identical conditions on silicon substrates with various seed densities and by comparing seed densities obtained by scanning electron microscopy to those determined by our strategy. We also explore the different deposition stages for which our model and a continuous film model can be used safely. In addition to providing guidelines for characterizing PCD deposition, this work may also advance the general understanding of nanoparticle growth and formation.

Received 19th October 2022
Accepted 1st December 2022

DOI: 10.1039/d2na00723a

rsc.li/nanoscale-advances

1 Introduction

1.1 Motivation and goals

According to Russell,¹ the term “incubation time”, which is used interchangeably with “incubation period”,² “induction time”,³ and “induction period”,⁴ describes thermally activated processes that do not commence immediately after establishing a reaction temperature. A prime example of a thermally activated process is the chemical vapor deposition (CVD) of polycrystalline diamond (PCD).⁵ Due to high activation energies associated with the nucleation of diamond grains on foreign substrates, relative to those of diamond deposition, incubation periods preceding deposition are observed.^{6–8} Such incubation periods can be reduced significantly, or even eliminated entirely, by seeding diamond nanoparticles, typically detonation nanodiamonds, on substrates before deposition.⁹ Still, the seeding step does not prevent incubation under certain deposition conditions.^{8,10,11} Incubation can be related to the etching of seeds,² which affects the seed density. Consequently, the morphological features of films and the physical properties

such as thermal conductivity, transparency, and adhesiveness are also affected.^{12–14} Incubation is mainly inferred from laser reflectance measurements. However, approaches to systematically obtain incubation periods and to gain information on properties that strongly affect film morphology, such as the areal density of seeds, from these measurements remain largely unexplored.

This work outlines a strategy for using laser reflectance measurements to estimate incubation periods, estimate the mean equivalent radii and the areal density of seeds, and refine the monitoring of film thickness during deposition. The specific goals of this work are to:

- Develop a semiquantitative, non-interference, and non-continuous film model for specular laser reflectance based on nanodiamond particle scattering that captures the early stages of PCD CVD on seeded substrates.
- Test our model experimentally by depositing diamond on substrates with different seed densities and by analyzing the samples with several microscopy techniques.
- Explore the different deposition stages for which our model and a continuous film model can be used safely.
- Develop a method to estimate incubation periods, which we identify with a delay in deposition and/or a reduced deposition rate during the early stages of deposition, with specular laser reflectance.

Mechanics and Materials Unit, Okinawa Institute of Science and Technology Graduate University, Okinawa, 904-0495, Japan. E-mail: eliot.fried@oist.jp; Tel: +81-98-966-1372

† Electronic supplementary information (ESI) available. See DOI: <https://doi.org/10.1039/d2na00723a>



For brevity, “specular laser reflectance” is shortened to “laser reflectance”. The term “diamond particle” refers to a single grain or to a cluster of grains isolated from other diamond particles and the term “seed” refers to a diamond particle deposited on the surface of a substrate before deposition.

1.2 Background

The small lattice parameter and the high surface energies of diamond limit diamond heteroepitaxy to diamond-on-iridium.^{15–20} An alternative method to deposit diamond on foreign substrates relies on seeding the substrate surface with diamond particles.^{21–28} Most work on seeding aims to increase the areal (seed) density with the objective of minimizing the thickness at which films become pinhole-free.^{29–31} However, high seed densities are not always desirable. For example, Mandal *et al.*³² found that a low seed density reduces stress in a PCD film grown on an aluminum nitride substrate, affording the deposition of a thicker film without delamination. Tsigkourakos *et al.*³³ found that lowering the seed density increases the electrical conductance of boron-doped films by one order of magnitude, and Janssens *et al.*³⁴ showed, through simulations, that the seed density strongly affects the grain size distribution. These results show that the seed density is a useful parameter for tuning the properties of PCD films and is therefore explored systematically in this work.

In situ laser reflectance interferometry is widely used for monitoring the thickness of a nanocrystalline diamond film during deposition. This is done by shining a laser beam on a sample, collecting the specularly reflected light with a photodetector, and analyzing the output signal that the photodetector produces.^{35–37} Fig. 1 shows a schematic of a reflectance setup installed on a CVD reactor. The film thickness and deposition rate are typically calculated from the extrema of the oscillating reflectance and the time intervals separating these extrema, respectively.^{4,38,39} The oscillations are caused by thin film interference.

In the early stage of diamond deposition on seeded silicon substrates, laser reflectance decays more slowly than expected for a continuous film.^{18,39} Some authors have related the initial slow decay of the reflectance to a reduced deposition rate or to the varying roughness of the sample surface.^{2,38} For the deposition of diamond on seeded substrates, the existence of incubation is mainly derived from the slow decay in reflectance during the early stages of deposition. However, it is not clear whether the estimation of an incubation period is strongly affected by the assumption of a continuous film. Here, we investigate this systematically by comparing laser reflectance with atomic force microscopy (AFM) and scanning electron microscopy (SEM).

Bonnot *et al.*⁴⁰ showed that during the early stages of PCD deposition, scattering from isolated diamond seeds increases with time. This increase was measured by installing a detector away from the specularly reflected laser. The analysis of the measured scattering was done using a model based on Rayleigh scattering, assuming that scattering caused by seeds is proportional to the square of their volume. This made it

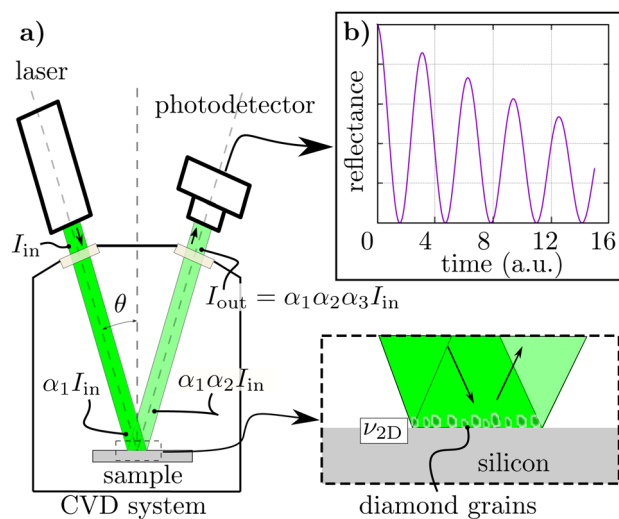


Fig. 1 Schematic of a reflectance setup. (a) Schematic of a setup for measuring the specular laser reflectance of a sample in a chemical vapor deposition (CVD) system during deposition. A laser beam of intensity I_{in} enters the CVD system at an angle θ . After interaction with the windows and the sample, the beam exits the system with intensity I_{out} . The arrows indicate the propagation direction of the laser beam. The windows cause attenuations α_1 and α_3 , and attenuation α_2 is caused by the sample. The detailed view of the dashed rectangle in (a) shows a schematic of diamond particles at the outset of deposition, with seed density ν_{2D} . (b) A typical graph obtained by plotting the photodetector's signal in (a) as a function of time. Regular oscillations, which are used for deposition rate estimation, are observed for thin-film interference.

possible to calculate the diamond deposition rate using scattering instead of reflectance. As demonstrated by Smolin *et al.*,⁴¹ Mie scattering, which generalizes Rayleigh scattering to large particles, can also explain the reflectance behavior during the initial stage of deposition. Smolin *et al.* measured reflectance by introducing a laser beam through a quartz window directed normal to the substrate surface and by measuring the specularly reflected beam intensity with a photodiode. However, the experiments reported in their work were limited by the control over seeding available at the time. Also, the implications of varying the diamond seed density on reflectance were not systematically investigated. These works demonstrate that light scattering, rather than interference, can accurately describe light-sample interactions during the early stages of PCD deposition. However, to the best of our knowledge, a relation that describes the reflectance during the early stages of PCD deposition has not yet appeared in the literature. Moreover, we are not aware of any previous attempt to include light scattering phenomena in the analysis of reflectance curves measured during incubation. We, therefore, develop an elementary model based on the Rayleigh theory of scattering to explain the behavior of laser reflectance during the early stages of PCD deposition and test the model experimentally.

Due to the non-interference nature of the light-sample interaction in the early stages of PCD deposition, we avoid using the term “laser reflectance interferometry” and opt for the more general term “laser reflectance”.



2 Model

2.1 Laser beam–sample interaction

A standard reflectance setup mounted on a CVD system is shown in Fig. 1. From linear optics, the attenuation α of a beam with intensity I_{in} entering the CVD system during diamond deposition is given by

$$\alpha = \frac{I_{\text{out}}}{I_{\text{in}}}, \quad (1)$$

where I_{out} is the intensity of the beam leaving the CVD system. Using the same argument for the beam intensity arriving and leaving the windows and sample, the total beam attenuation can be expressed as

$$\alpha = \alpha_1 \alpha_2 \alpha_3, \quad (2)$$

where α_1 and α_3 are the beam attenuation caused by the windows and α_2 is the attenuation caused by the sample. The absolute specular reflectance is the ratio of the beam intensity leaving the sample to that arriving at the sample. Following this definition, α_2 can be identified with the absolute specular reflectance of the sample consisting of diamond particles on a silicon surface. We therefore write α_2 as the product of the attenuation α_{21} caused by scattering due to diamond particles and the absolute specular reflectance α_{22} of the silicon substrate:

$$\alpha_2 = \alpha_{21} \alpha_{22}. \quad (3)$$

We then define the relative reflectance R through

$$R = \frac{\alpha_2}{\alpha_{22}} = \alpha_{21}. \quad (4)$$

The voltage measured by the photodetector, as depicted in Fig. 1a, is proportional to the responsivity r of the detector. Dividing the voltage V measured in the presence of diamond particles by the voltage V_0 measured for a bare silicon substrate, we obtain the relative voltage

$$\frac{V}{V_0} = \frac{r \alpha_1 \alpha_{21} \alpha_{22} \alpha_3 I_{\text{in}}}{r \alpha_1 \alpha_{22} \alpha_3 I_{\text{in}}} = \alpha_{21}. \quad (5)$$

From (4) and (5), we find that the relative voltage V/V_0 equals R , which is entirely determined by the attenuation due to scattering by diamond particles. We also note that these results are applicable only when the specularly reflected beam intensity is much larger than the scattered intensity in the direction of the detector. This condition is fulfilled for a polished substrate with a high refractive index on which relatively small nanoparticles are present.

2.2 Scattering caused by a collection of particles constrained in a plane

To obtain a relation for α_{21} , we first recognize that the intensity change, per unit length, dI/dz of a beam with initial intensity I_0 traveling in a non-absorbing host fluid containing particles with number density per unit volume ν can be expressed as

$$\frac{dI}{dz} = -I_0 \nu \sigma, \quad (6)$$

where σ denotes the scattering cross-section of the particles in the fluid. The Rayleigh approximation can be written as $\lambda_0 \gg 2a$, where λ_0 is the wavelength of the incoming beam in the host fluid and a the radius of the suspended particles. In the Rayleigh approximation, the scattering cross-section σ_{R} is given by

$$\sigma_{\text{R}} = \frac{8\pi}{3} \left(\frac{2\pi n_{\text{g}}}{\lambda_0} \right)^4 a^6 \left(\frac{m^2 - 1}{m^2 + 2} \right)^2, \quad (7)$$

with $m = n_{\text{p}}/n_{\text{g}}$, where n_{p} and n_{g} are the refractive indices of the particles and the host fluid respectively.⁴² When the particles are constrained to a plane, as shown in Fig. 2, the change ΔI in intensity I for a beam traveling through the particles is written as

$$\Delta I = -I_0 \nu_{2\text{D}} \sigma_{\text{R}}, \quad (8)$$

where $\nu_{2\text{D}}$ is the density of particles. The beam intensity I after interaction with the particles is thus given by

$$I = I_0 + \Delta I = I_0(1 - \nu_{2\text{D}} \sigma_{\text{R}}). \quad (9)$$

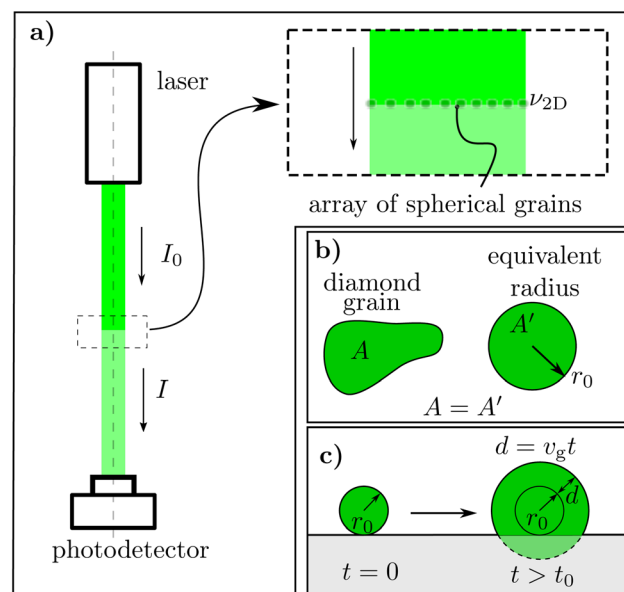


Fig. 2 Model for calculating scattering caused by growing diamond particles. (a) Schematic of an imaginary experimental setup to calculate the scattering caused by a collection of uniform size diamond particles constrained to a plane. The beam exits the laser with intensity I_0 , and the intensity after interaction with the particles is reduced to I . The particles are assumed to be spherical and of the same radius a . (b) To obtain a experimentally, we measure the projected area A of a diamond particle, calculate the radius r of the circle with area A' for which $A = A'$, and take the mean value of r for all the particles. (c) Uniform deposition on an equivalent seed with radius a_0 at the outset of the deposition is depicted. The radius of the particle is the sum of a_0 and the deposited thickness d . The deposited thickness is expressed as $d = v_{\text{d}} t$, with v_{d} and t denoting deposition rate and deposition time, respectively.



A beam with oblique incidence at angle θ interacts with an effective density of particles given by $v_{2D}/\cos\theta$. Replacing v_{2D} in (9) with $v_{2D}/\cos\theta$ and dividing by I_0 , we observe that the attenuation of this beam after interaction with a collection of particles constrained on a plane can be expressed as

$$\frac{I}{I_0} = 1 - \beta \frac{v_{2D}}{\cos\theta} a^6, \quad (10)$$

where β is defined by

$$\beta = \frac{8\pi}{3} \left(\frac{2\pi n_g}{\lambda_0} \right)^4 \left(\frac{m^2 - 1}{m^2 + 2} \right)^2.$$

Relation (10) is valid for a collection of isolated, relatively small, and uniformly sized spherical particles. However, in processes of interest here, seeds are randomly positioned on the silicon substrate after seeding, and their size is not uniform. Also, diamond particles grow homoepitaxially from the seeds and coalesce during deposition, which affects v_{2D} . Without performing a complete statistical analysis of the growth and coalescence of diamond particles, we model the relative reflectance R in the initial stages of diamond deposition using $\alpha_{21} = I/I_0$ and assuming that:

- The diamond particles are sufficiently small to ensure that the Rayleigh approximation applies.
- Particle clustering, which reduces particle density, can be ignored.
- Diamond particles can be represented by uniformly sized spheres of radius a . The method for obtaining a experimentally is described in Fig. 2b and its caption.
- The particle size increases uniformly. Consequently, the radius a increases as

$$a = a_0 + d, \quad (11)$$

with a_0 and d denoting the mean equivalent radius of seeds and the deposited thickness, respectively, as illustrated in Fig. 2c. The thickness d is expressed as

$$d = v_d t, \quad (12)$$

with v_d and t denoting the deposition rate and deposition time, respectively.

With these provisions, the length a in (10) represents the mean equivalent radius of a collection of diamond particles. Using (10) in (4), we obtain

$$R = 1 - \beta \frac{v_{2D}}{\cos\theta} a^6. \quad (13)$$

With the fourth assumption listed above, the particle radius at time t is given by

$$a = a_0 + v_d t. \quad (14)$$

Substituting (14) in (13), we obtain the representation for R , namely

$$R = 1 - \beta \frac{v_{2D}}{\cos\theta} (a_0 + v_d t)^6, \quad (15)$$

which facilitates comparisons with data from reflectance measurements.

3 Experiment

Diamond deposition was performed on 2×2 cm silicon substrates cleaved from 100 mm diameter phosphorus-doped silicon wafers with a resistivity of 1–10 Ω cm obtained from Electronics and Materials Corporation, Limited. After cleaving, the substrates were cleaned by a sequential ultrasonic bath in deionized (DI) water, acetone, isopropanol, and DI water for 5 min each. The substrates were then immersed for 10 min in Semiclean solution obtained from Furuuchi Chemical Corporation, rinsed in DI water, and dried with high purity nitrogen. After the cleaning process, the substrates were exposed to an air plasma in a PR200 Plasma reactor obtained from Yamato Scientific Corporation, Limited to improve the wettability of their surfaces. The plasma power and exposure time were set to 170 W and 60 s, respectively, and the airflow rate was kept at 100 sccm. Immediately after the plasma treatment, the substrates were transferred to a spin coater, where they were seeded with suspensions of various nanodiamond concentrations. Cleaning and seeding were done without pause to avoid airborne surface contamination affecting the seeding.⁴³ The seeding procedure was done by drop casting 150 μ L of nanodiamond suspension on an immobile substrate. One minute after drop casting the suspension, the sample was spun at a rotation speed of 6000 rpm for 30 s while flushing the wetted surface with DI water for the first 5 s of spinning.

Nanodiamond suspensions were made by dispersion of NanoAmando Hard Hydrogel detonated nanodiamond powder obtained from NanoCarbon Research Institute Corporation, Limited in 0.2 L of DI water at a proportion of 0.5 g L⁻¹, and ultrasonication of the mixture with an Epishear probe sonicator with tip diameter 3.2 mm and length 4.5 cm. This was achieved using an ultrasonic transducer with a power of 100 W and a frequency of 20 kHz. To avoid overheating the system, an on/off cycle of 1 s/1 s was fixed for 90 min. The obtained suspension was centrifuged at 15 000 rpm for 30 min to remove large agglomerates of more than 140 nm. The supernatant was recovered and diluted with DI water to obtain concentrations of 10–60% with respect to the as-centrifuged supernatant concentration of 100%.

Diamond was deposited on the seeded substrates using an SDS6500X microwave plasma-assisted CVD system from Cornes Technologies. For all samples, PCD was deposited with a plasma power of 1500 W, a hydrogen flow rate of 288 sccm, a methane flow rate of 12 sccm, and a chamber pressure of 15 torr. This was done using programmed recipes to ensure repeatability. The microwaves and the plasma in the CVD chamber heated the substrate. The temperature of each sample was found to stabilize at 530 ± 8 °C, as measured by an FLHX-PNE0300 infrared thermometer with a spectral range of 0.6–1.8 μ m from Japan Sensor Corporation with emissivity set to 0.6. The deposition was monitored *in situ* by a homemade laser reflectance setup consisting of a 1 mW power semiconductor laser emitting at 532 nm that was directed to the sample



through a viewport in the CVD chamber at angle θ equal to approximately 20° . A schematic of this setup is provided in Fig. 1a. A silicon photodetector collected the reflected light from the substrate surface. A laser line filter centered at 532 nm with an FWHM of 1 nm was positioned between the viewport and the silicon photodetector to avoid plasma emission from reaching the photodetector.

The measured deposition rate was $0.6 \pm 0.05 \text{ nm min}^{-1}$ obtained by growing a reference sample for 5 h. The thickness of the calibration layer was 180 nm, as measured with an optical nanogauge C13027-11 obtained from Hamamatsu Photonics and corroborated by cross-section scanning electron microscopy (SEM) observation. Seeded substrates were characterized using a JEOL JSM-7900F scanning electron microscope obtained from JEOL. Analysis of the SEM images was automated by a Python (<https://www.python.org>) script that makes use of the Image-J (<https://imagej.net/Fiji>) bandpass filter to denoise the original images and the OpenCV “findContours()” function for the particle analysis. The number density ν_{2D} is the number of isolated particles recognized by the Python script and averaged over five images at $50\,000\times$ magnification from different portions on the substrates. After the deposition, the samples were characterized by atomic force microscopy (AFM) on an Agilent 5500 scanning probe microscope obtained from Keysight Technologies using silicon probes with 7 nm nominal radius, 14 μm nominal cantilever length, a nominal cantilever resonance frequency of 300 kHz and a 26 N m^{-1} spring constant. AFM image analysis and profile extraction were done using Gwyddion (<https://gwyddion.net>). Statistical analysis of particle size was done by particle marking using the “watershed” method.⁴⁴

4 Results and discussion

4.1 Predictions of the model

To understand the implications of our model, we plot the relative reflectance R versus t using the Rayleigh scattering relation (15) for various choices of ν_d with $a_0 = 20 \text{ nm}$ and $\nu_{2D} = 1 \times 10^{10} \text{ cm}^{-2}$. Fig. 3a shows that R decays more slowly as ν_d decreases. To avoid confusing this effect with the presence of incubation, we use (12) and (15) to express R in terms of d :

$$R = 1 - \beta \frac{\nu_{2D}}{\cos \theta} (a_0 + d)^6. \quad (16)$$

Using (16), the reflectance data in Fig. 3a collapses onto the dashed curve in Fig. 3b, where R is plotted as a function of d . In Fig. 3b R is also plotted for other values of ν_{2D} . The black curve corresponds to R of a continuous diamond film calculated by the transfer-matrix method.⁴⁵ The colored curves exhibit less decay than the black curve as d increases. Guided by the horizontal dotted line at a fixed value of R , and assuming that our model correctly predicts R as a function of d , we deduce that an experimenter would underestimate the value of d using the continuous film model during the early stages of deposition. Consequently, film thickness and deposition rate are also underestimated with the continuous film model, and the presence of an incubation period might falsely be deduced. Low

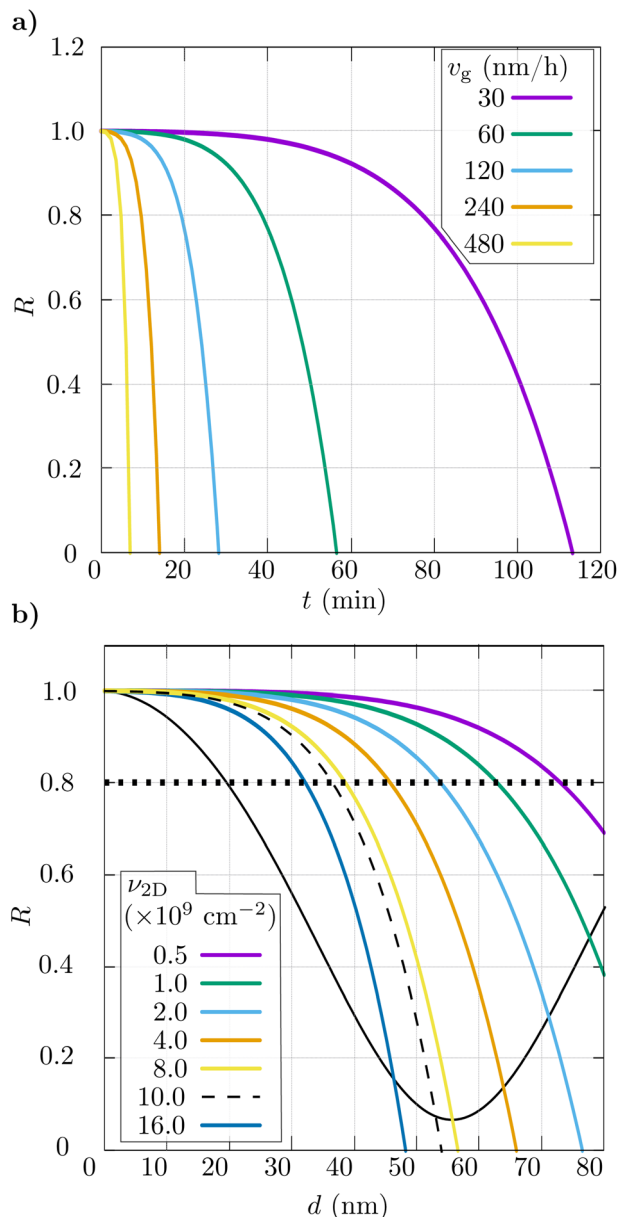


Fig. 3 Simulated reflectance during diamond deposition. (a) Relative reflectance R calculated using (15) for diamond deposition on seeded substrates as a function of deposition time t for various deposition rates. (b) R calculated using (16) as a function of deposited thickness d for various values of ν_{2D} . Radius a_0 was set to 20 nm for all calculations. The black curve in (b) corresponds to the normalized reflectance for a continuous diamond film calculated by the transfer-matrix method.⁴⁵

values of ν_{2D} cause less scattering than high values, which explains the slower decay of R as ν_{2D} decreases.

In a review on nanocrystalline diamond by Williams,² R is plotted as a function of t for diamond deposition on seeded substrates. The reflectance curves exhibit a decay that reduces as the methane concentration in the gas phase reduces. This trend is reasoned to be caused by an extension of the incubation period as the methane concentration is reduced. However, by assuming that ν_d is proportional to the methane



concentration, a possible alternative explanation is that a reduced methane concentration produces a lower deposition rate that delays the reflectance decay. The reality is probably a combination of both descriptions since a plasma with lower methane concentration might etch grains, leading to incubation. To resolve the ambiguity regarding the existence of incubation, we refer to a method delineated in our previous work⁸ for estimating incubation periods. In Section 4.3, we extend this method.

4.2 Experimental verification of the model

We test our model by comparing the relative reflectance R during diamond deposition on seeded substrates with various values of ν_{2D} . The values of ν_{2D} and a_0 were obtained by SEM analysis. The Rayleigh scattering relation (15) was fitted to the reflectance curves obtained during diamond deposition using the parameters ν_{2D} , a_0 , and V_0 . The values of ν_{2D} and a_0 were compared with those obtained from SEM. After deposition, the surface morphology of the samples was analyzed by AFM. Finally, the height distributions of diamond particles were correlated to the reflectance measurements.

4.2.1 Seeding. The SEM images in Fig. 4a and b show substrates seeded using suspensions of concentration $x = 10\%$ and $x = 100\%$, respectively, from which we observe that the surface coverage and ν_{2D} increase as x increases. Fig. 4c reveals that this increase is linear for the surface coverage in the full range, and linear for ν_{2D} up to 60%. We speculate that the deviation of ν_{2D} from the linear behavior observed at 100% is caused by agglomeration and the limited resolution of the SEM, which make it challenging to resolve seeds in close proximity. These results show that our seeding procedure enables control over ν_{2D} . A complete set of images of seeded substrates is shown in Fig. S1 in the ESI.† The figure also includes images after particle analysis with contours drawn around the detected seeds.

In the work of Tsigkourakos *et al.*³³ the surface coverage was found to vary non-linearly for suspension concentrations in the range of 0.002 g L^{-1} to 2 g L^{-1} . Recognizing that nanodiamonds in suspension tend to aggregate relatively fast at low concentrations,⁴⁶ we hypothesize that nanodiamond agglomerates were seeded in that work. Scorsone *et al.*²⁹ obtained good linearity between ν_{2D} and nanodiamond concentration in the suspension. Still, the suspension preparation required the addition of polyvinyl alcohol and ultrasonication at $40 \text{ }^\circ\text{C}$ for 2 h. In the work described here, we simply diluted a stock suspension immediately before seeding to avoid dilution-induced agglomeration.

4.2.2 Reflectance during the early stages of diamond deposition. The relative reflectance R measured during diamond deposition on samples seeded with suspensions of various x is shown in Fig. 5 as a function of d . The dashed black lines in Fig. 5 are obtained by fitting the alternative representation (15) for R to the data, and are discussed hereinafter. Three time intervals can be identified in each plot: (i) the onset of deposition, (ii) deposition, and (iii) end of the deposition. The onset of deposition comprises the interval starting at the

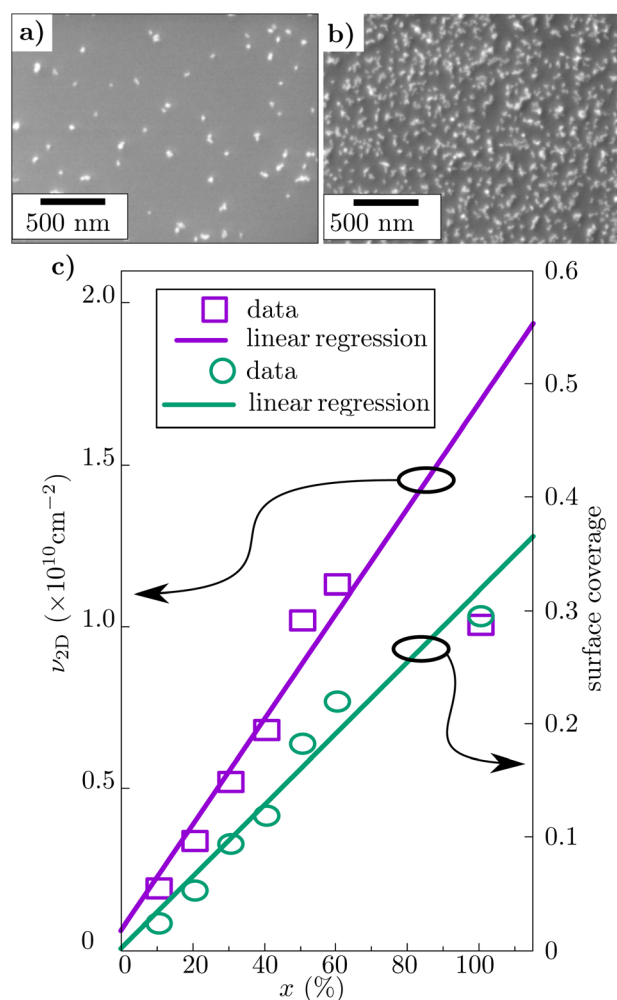


Fig. 4 Seed density. (a) SEM image of a sample seeded using a suspension of concentration $x = 10\%$. (b) SEM image of a sample seeded with an $x = 100\%$ suspension. (c) Seed density ν_{2D} and surface coverage as function of x . Density ν_{2D} is defined as the number of isolated diamond particles in the image, divided by the total area. For the linear regression the value of ν_{2D} for $x = 100\%$ is not considered.

ignition of the plasma and finishing when the substrate temperature reaches $530 \text{ }^\circ\text{C}$. This time interval, typically about 5 min, begins and ends in the positions indicated by blue and green vertical dashed lines, respectively. The end of deposition starts when the plasma power is deactivated. During this time interval, the substrate experiences a sudden drop in temperature, which is driven by the cooled stage of the CVD system. The deposition interval occurs between the onset of the deposition interval and the end of the deposition interval. A relatively small ν_d of 0.6 nm min^{-1} was selected to guarantee that deposition outside the deposition interval can be safely neglected.

As predicted by our model, the decay of R as a function of d is inversely proportional to ν_{2D} . In contrast to findings reported in the existing literature, our measurements show that a diminished decay of R is not *per se* related to incubation. Evidence for incubation is mainly based on literature^{2,4} that describes polycrystalline diamond deposition by the bias-enhanced



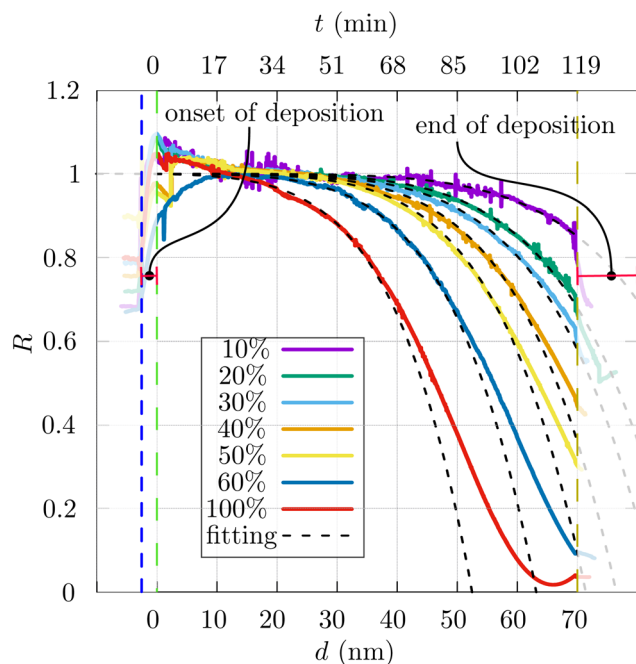


Fig. 5 Experimental and simulated reflectance curves. Laser reflectance R as a function of the deposition time t and the deposited thickness d . R is monitored during the deposition of diamond on silicon substrates seeded with nanodiamond suspension of concentrations ranging from 10% to 100% relative to the stock suspension. The dashed black curves correspond to fitting (15) to the experimental curves. The green and dark yellow vertical dashed lines indicate the start and end of the deposition, respectively. The blue dashed line indicates the time at which the plasma is ignited.

nucleation method. Stoner⁴ found that in the initial stage of diamond deposition, by this method, incubation is observed, during which no diamond deposition occurs. This has been corroborated by Jiang *et al.*³ using AFM measurements which showed that diamond nuclei were not created until after 6.5 min of plasma exposure. In the works of Stoner and Jiang *et al.*, incubation is ascribed to diamond nucleation that starts after the silicon substrate is saturated with carbon. For polycrystalline diamond deposition on seeded substrates under harsh conditions, we previously showed that incubation is present due to seed etching.⁸ However, under mild conditions similar to those used in this work, incubation has never been corroborated (to the best of our knowledge).^{47,48}

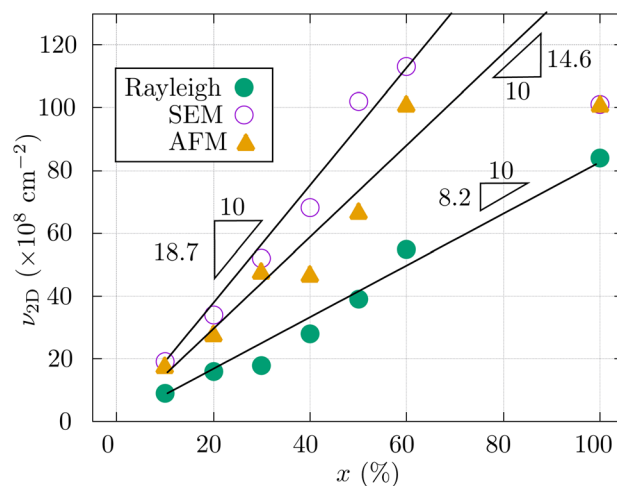


Fig. 6 Estimated diamond particle densities. Diamond particle density ν_{2D} , as a function of the concentration x , obtained by (i) fitting the Rayleigh scattering relation (15) to the reflectance curves displayed in Fig. 5, (ii) the SEM image analysis that is delineated in Section 4.2.1 (before deposition), and (iii) AFM particle marking that is delineated in Section 4.2.3 (after deposition). For the linear regression, the values of ν_{2D} at 100% obtained by SEM and AFM are not considered.

Quantitative results are obtained by non-linear least-square fitting of (15) with the values $\nu_d = 0.6 \text{ nm min}^{-1}$, $n_p = 2.41$, $n_g = 1$, and $\lambda_0 = 532 \text{ nm}$ and fitting parameters ν_{2D} , a_0 , and V_0 . The fitting ranges are manually adjusted and are listed in Table 1. From the dashed curves in Fig. 5, we observe that the fits for samples seeded using low-concentration diamond suspensions are good over the entire deposition interval. However, the fits and the experimental data diverge for high concentrations before the deposition ends. This can be attributed to the proximity of neighboring particles for samples with high seed densities. When the radius of a diamond particle exceeds half of the distance to its nearest neighbor, they coalesce and form a larger particle. This phenomenon has two consequences:

(1) The diamond particle density ν_{2D} will be reduced due to coalescence.

(2) Coalesced particles may be larger than the wavelength for which the Rayleigh scattering approximation holds, leading to significant discrepancies between the model and the experimental data.

Table 1 Nanodiamond seed densities and mean equivalent radius, measured by SEM analysis and estimated by fitting (14) to the experimental data in Fig. 5. The fitting range for all samples is also included

Sample%	ν_{2D} (SEM) $\times 10^9 \text{ cm}^{-2}$	a_0 (SEM) nm	ν_{2D} (fitting) $\times 10^9 \text{ cm}^{-2}$	a_0 (fitting) nm	Fitting range d nm
10	1.9	19	0.9	10	10–69
20	3.4	20	1.6	13	10–67
30	5.2	22	1.8	14	10–65
40	6.8	21	2.8	14	10–63
50	10.2	21	3.9	14	10–61
60	11.3	22	5.5	18	10–41
100	10.1	27	8.4	23	10–29



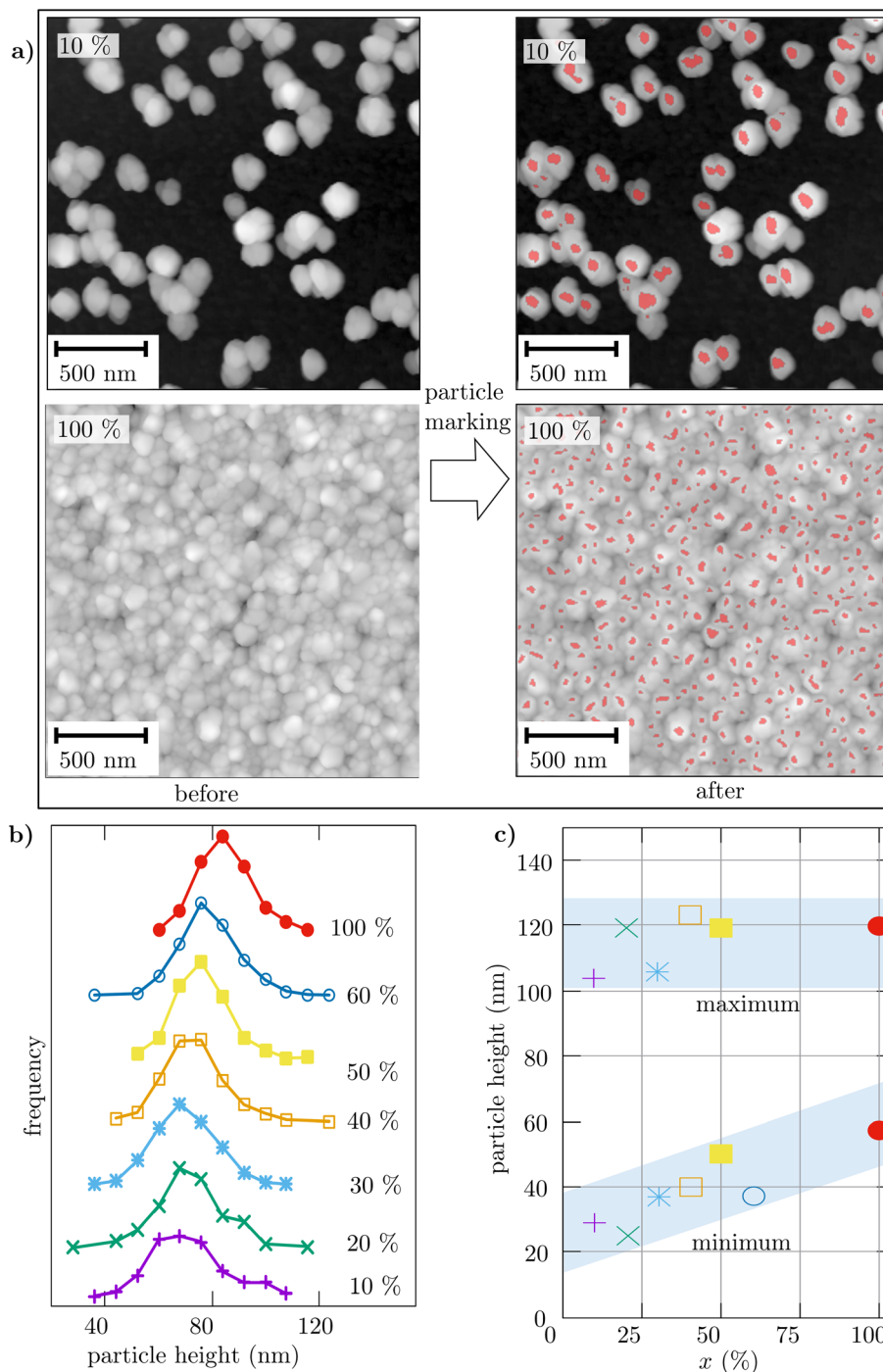


Fig. 7 AFM particle analysis. (a) AFM images of samples seeded with suspensions of concentration $x = 10\%$ and $x = 100\%$, before and after applying the watershed method for marking particles. (b) Height distribution and (c) the maximum and the minimum height of particles found in the analysis of two AFM images of each sample.

Once all diamond particles coalesce to form a continuous layer of polycrystalline diamond, which we called the closed-film threshold in our previous work,³⁴ the reflectance signal can be described using the transfer matrix method.⁴⁵ By visual inspection, it is also evident that the fitting curves coincide with experimental data up to a reflectance value of 0.7 ± 0.1 , which

we interpret as the empirical reflectance limit above which our model can be applied with confidence.

Values for ν_{2D} obtained by fitting the curves in Fig. 5 are shown in Table 1 and values for ν_{2D} estimated by SEM analysis in Section 4.2.1 are also shown for comparison. Fig. 6 shows that except for the sample grown on the substrate seeded with the 100% concentration suspension, the values for ν_{2D} obtained



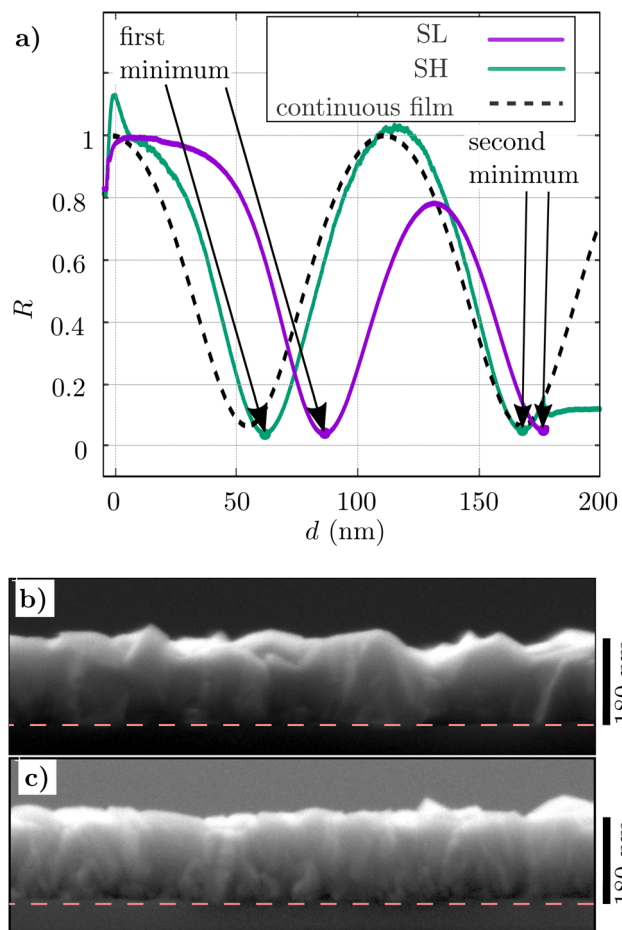


Fig. 8 Film deposition after the early stages of deposition. (a) Reflectance data measured during diamond deposition plotted versus deposited thickness d of samples SL and SH with seed density ν_{2D} equal to $1.00 \times 10^{10} \text{ cm}^{-2}$ and $2.95 \times 10^{10} \text{ cm}^{-2}$, respectively. The plots show that after depositing 180 nm of diamond, the positions of the minima tend to the same value of d . (b) and (c) Show SEM cross-sections of SL and SH, respectively. Both images show that SL and SH have similar thicknesses (180 nm), but the RMS surface roughness of SL appears larger than that of SH. A red dashed line in (b) or (c) indicates the substrate–diamond interface.

by SEM analysis are proportional to those obtained by fitting using the Rayleigh scattering relation (15) with a proportionality constant of 0.44.

4.2.3 Seed density versus deposition rate. Our model hinges on the assumptions that the deposition rate ν_d (i) is constant during deposition, and (ii) is independent of the particle density ν_{2D} . The former assumption is supported by experiments in this work and can also be inferred from Fig. 4 in the work of Leigh and coworkers.⁴⁹ In our work, particle height statistics were performed on AFM data to assess the validity of the latter assumption. We obtained statistical information from the height of the particles by the “watershed” method.⁴⁴ This method allows for marking particles based on height local minima/maxima in an AFM image; thereby, coalesced particles forming clusters or forming a film can be identified as individual particles. The particle density, the height distribution, the maximum particle height, and the minimum particle height

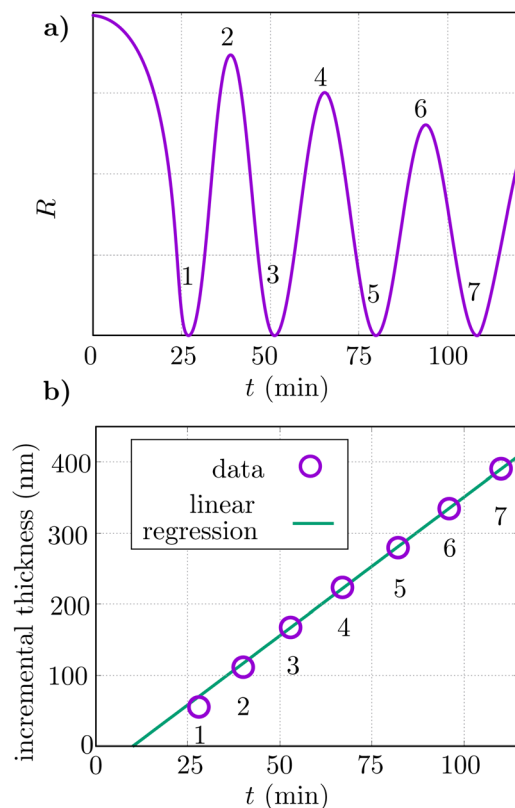


Fig. 9 Schematic reflectance to depict the method to estimate the incubation period. (a) Typical reflectance R curve obtained during diamond deposition on seeded substrates as a function of time t where extrema are numbered. (b) Incremental thickness h as a function of t for the curve in (a). The values of h are calculated with (17).

for each sample were obtained by analyzing AFM data from two areas measured at different positions. In Fig. 6, the values of ν_{2D} obtained by SEM and AFM, before and after deposition, respectively, are plotted as functions of the concentration x of diamond particles in solution. The smaller slope obtained from AFM is caused by grain burying, as explained in the following paragraph.

Fig. 7a contains examples of AFM images before and after particle marking. A complete set of images can be found in Fig. S2 of the ESI.† The particle height distributions are shown in Fig. 7b, and the maximum and minimum height as a function of x are provided in Fig. 7c. From this data, we find that (i) the particle height at the maximum frequency increases as x increases, (ii) the maximum height ($114 \pm 10 \text{ nm}$) is not significantly dependent on x , and (iii) the minimum height increases as x increases. These findings can be explained as follows. During deposition, smaller particles are buried by larger particles.⁵⁰ Burying occurs more frequently as ν_{2D} increases because the mean distance between particles decreases as ν_{2D} increases. Consequently, the particle height at the maximum frequency and the minimum particle height shift towards larger values. In this scenario, the particle of maximum height is not affected by burying and its height is independent



of ν_{2D} provided that ν_d is constant for all the samples, as we assume to be so.

4.3 Seed density versus mean film thickness

Since surface roughness decreases after film closure³⁸ and the maximum grain height is independent of ν_{2D} , as shown in Section 4.2.3, the mean film thickness should become less dependent on ν_{2D} as the deposited thickness increases. As a consequence, we hypothesize that the R curves for samples grown on a substrate with dissimilar ν_{2D} should show extrema at values of d that become more similar as d increases. Using Fig. 8a, we test this hypothesis by comparing R as a function of d for samples SL and SH with $\nu_{2D} = 1.00 \times 10^{10} \text{ cm}^{-2}$ and $\nu_{2D} = 2.95 \times 10^{10} \text{ cm}^{-2}$, respectively, as measured by SEM. While the R curve for SL exhibits the first minimum at approximately $d = 86.0 \text{ nm}$, the first minimum for the R curve of SH is at approximately $d = 61.5 \text{ nm}$. On the other hand, the position of the second minimum is about $d = 178 \text{ nm}$ and $d = 168 \text{ nm}$ for SL and SH, respectively. The difference in d for the second minimum is only 10 nm, which is considerably smaller than the 24.5 nm observed for the first minimum and, therefore, supports our hypothesis.

Fig. 8b and c show the SEM cross-section of SL and SH, respectively. From these cross-sections, we deduce that the mean film thickness is similar in both samples, which is in line with SL thickness 182 nm and SH thickness 184 nm that we obtained by an optical nanogauge. From these cross sections, we also observe that the surface of SL is rougher than that of SH. We verify and quantify this by analyzing AFM data, obtained from two $5 \times 5 \mu\text{m}^2$ areas measured at different positions, for each sample. AFM images from these samples and their profiles along the selected lines are shown in Fig. S3 of the ESI.† The result of the analysis is 14.6 nm and 11.0 nm RMS surface roughness for SL and SH, respectively. This difference in surface roughness might contribute to the difference in d for the second minima in Fig. 8a. In addition to surface roughness, we hypothesize that voids at the substrate–film interface might also contribute to this difference.

The results presented in the present section also show that even for a relatively low value of ν_{2D} , the continuous film model can provide a reasonable approximation of the mean film thickness beyond the early stages of deposition.

4.4 Estimation of incubation periods by laser reflectance

To systematically obtain an incubation period and the deposition rate by laser reflectance, we use the findings presented in this work to extend a previously proposed method.⁸ To quantify the incubation period, we collect the values of t where the extrema in R occur. A schematic of such a curve is provided in Fig. 9a. Subsequently, we estimate the incremental thickness $h = l\Delta h$, which we define as the thickness at the l^{th} extremum, calculated for a continuous film. The thickness Δh is a constant that can be calculated with the relations

$$\Delta h = \frac{\lambda_0}{4n_{\text{Dia}} \cos \gamma}, \quad \gamma = \arcsin\left(\frac{\sin \theta}{n_{\text{Dia}}}\right), \quad (17)$$

where n_{Dia} is the refractive index of diamond, assuming that the surrounding medium is vacuum with a refractive index equal to unity. Corresponding pairs of h and t are then plotted as illustrated in Fig. 9b. Finally, we perform a linear regression with all the data points except those corresponding to the first two extrema. From Section 4.3, we derive that the values of h corresponding to the first two extrema are not well-described by the continuous film model. These extrema should therefore be avoided, especially for low values of ν_{2D} . The intercept with the t -axis and the slope, both obtained by linear regression, are the incubation period and deposition rate, respectively.

In the event that few or no extrema are observed, more sophisticated characterization techniques such as “specific zone marking”,³⁶ that enable the observation and measurement of localized diamond particles before and after diamond deposition, can be used.

5 Conclusions

The chemical vapor deposition of polycrystalline diamond (PCD) films is typically done on substrates seeded with diamond nanoparticles. In this work, we outlined a strategy for using laser reflectance measurements to refine the monitoring of film thickness during deposition, estimate the mean equivalent radii and the areal density of seeds, and estimate growth incubation periods. We presented a simple model to describe specular laser reflectance in the early stages of PCD deposition. The reflectance behavior predicted by our model differed from that of a continuous film, which is well-described by a continuous film model, and this difference enlarged as the seed density used in our model decreased. These predictions were tested and confirmed by *in situ* specular laser reflectance measurements of diamond deposition on silicon substrates with various seed densities. A relation for reflectance found in our model was fitted to the experimental reflectance data, and the seed density obtained by fitting was found to be proportional to the seed density obtained by scanning electron microscopy analysis. Post-deposition atomic force microscopy data analysis showed that the deposition rate is independent of the seed density, which supports an assumption made in our model. Other deposition experiments showed that the continuous film model can be used safely beyond the early stages of deposition. We also showed that relying on the continuous film model for describing the early stages of deposition can result in questionable conclusions regarding the presence of incubation or the duration of incubation periods. Inspired by this, we proposed a method for estimating incubation periods together with a deposition rate, based on laser reflectance measurements. Our work provides guidelines for using laser reflectance as a tool to elucidate and guide the deposition of PCD films with tailored properties. Our work may also advance the general understanding of nanoparticle growth and formation.

Conflicts of interest

There are no conflicts to declare.



Nomenclature

a	Mean equivalent radius
a_0	Mean equivalent radius of diamond seeds
α	Total beam attenuation caused by the CVD system
α_1	Beam attenuation caused by entering the CVD system
α_2	Beam attenuation caused by the sample
α_{21}	Beam attenuation caused by the diamond particles on the silicon substrate
α_{22}	Beam attenuation caused by the total reflectance of the silicon substrate
α_3	Beam attenuation caused by exiting the CVD system
β	$\frac{8\pi}{3} \left(\frac{2\pi n_g}{\lambda_0}\right)^4 \left(\frac{m^2 - 1}{m^2 + 2}\right)^2$
d	Deposited thickness
σ	Scattering cross section
σ_R	Rayleigh scattering cross section
I_0	Beam intensity before interaction with small particles
I	Beam intensity
I_{in}	Beam intensity entering the CVD system
I_{out}	Beam intensity leaving the CVD system
l	Sequence number of an extremum
λ_0	Beam wavelength in the medium
m	Ratio n_p/n_g
n_g	Refractive index of the medium
n_p	Refractive index of the particles
ν	Number density per unit volume
ν_{2D}	Nanodiamond seed density
R	Relative reflectance
r	Equivalent radius
t	Time
θ	Angle of incidence
V	Voltage measured during diamond deposition
V_0	Voltage for a beam reflected on a bare silicon substrate
ν_d	Deposition rate
x	Suspension concentration

Acknowledgements

The authors thank the Okinawa Institute of Science and Technology Graduate University (OIST) for the financial support, with subsidy funding from the Cabinet Office, Government of Japan. The authors also thank T. Sasaki, from the Scientific Imaging Section at OIST, for the assistance and technical guidance on SEM measurements. S. D. J. and E. F. acknowledge JSPS KAKENHI funding grant number JP21K03782, and B. S. acknowledge JSPS KAKENHI (Grants-in-Aid for Early-Career Scientists) grant number JP20K15347.

References

- 1 K. C. Russell, Grain boundary nucleation kinetics, *Acta Metall.*, 1969, **17**, 1123–1131.
- 2 O. A. Williams, Nanocrystalline diamond, *Diamond Relat. Mater.*, 2011, **20**(5), 621–640.
- 3 X. Jiang, K. Schiffmann and C.-P. Klages, Nucleation and initial growth phase of diamond thin films on (100) silicon, *Phys. Rev. B: Condens. Matter Mater. Phys.*, 1994, **50**, 8402–8410.
- 4 B. R. Stoner, B. E. Williams, S. D. Wolter, K. Nishimura and J. T. Glass, In situ growth rate measurement and nucleation enhancement for microwave plasma CVD of diamond, *J. Mater. Res.*, 1992, **7**(2), 257–260.
- 5 J. E. Butler and A. V. Sumant, The CVD of nanodiamond materials, *Chem. Vap. Deposition*, 2008, **14**(7–8), 145–160.
- 6 K. A. Snail and C. M. Marks, In situ diamond growth rate measurement using emission interferometry, *Appl. Phys. Lett.*, 1992, **60**(25), 3135–3137.
- 7 A. Yamaguchi, M. Ihara and H. Komiyama, Temperature dependence of growth rate for diamonds grown using a hot filament assisted chemical vapor deposition method at low substrate temperatures, *Appl. Phys. Lett.*, 1994, **64**(10), 1306–1308.
- 8 A. Giussani, S. D. Janssens, D. Vázquez-Cortés and E. Fried, Evolution of nanodiamond seeds during the chemical vapor deposition of diamond on silicon substrates in oxygen-rich plasmas, *Appl. Surf. Sci.*, 2022, **581**, 152103.
- 9 S. Iijima, Y. Aikawa and K. Baba, Early formation of chemical vapor deposition diamond films, *Appl. Phys. Lett.*, 1990, **57**(25), 2646–2648.
- 10 S. Stehlik, M. Varga, P. Stenclova, L. Ondic, M. Ledinsky, J. Pangrac, O. Vanek, J. Lipov, A. Kromka and B. Rezek, Ultrathin nanocrystalline diamond films with silicon vacancy color centers via seeding by 2 nm detonation nanodiamonds, *ACS Appl. Mater. Interfaces*, 2017, **9**(44), 38842–38853.
- 11 A. Kromka, Š. Potocký, J. Čermák, B. Rezek, J. Potměšil, J. Zemek and M. Vaněček, Early stage of diamond growth at low temperature, *Diamond Relat. Mater.*, 2008, **17**(7), 1252–1255. Proceedings of Diamond 2007, the 18th European Conference on Diamond, Diamond-Like Materials, Carbon Nanotubes, Nitrides and Silicon Carbide.
- 12 Y.-C. Lee, S.-J. Lin, C.-Y. Lin, M.-C. Yip, W. Fang and I.-N. Lin, Pre-nucleation techniques for enhancing nucleation density and adhesion of low temperature deposited ultrananocrystalline diamond, *Diamond Relat. Mater.*, 2006, **15**(11), 2046–2050. Proceedings of the Joint 11th International Conference on New Diamond Science and Technology and the 9th Applied Diamond Conference 2006.
- 13 J. Anaya, T. Bai, Y. Wang, C. Li, M. Goorsky, T. L. Bougher, L. Yates, Z. Cheng, S. Graham, K. D. Hobart, T. I. Feygelson, M. J. Tadjer, T. J. Anderson, B. B. Pate and M. Kuball, Simultaneous determination of the lattice thermal conductivity and grain/grain thermal resistance in polycrystalline diamond, *Acta Mater.*, 2017, **139**, 215–225.
- 14 L. Huang, T. Wang, X. Li, X. Wang, W. Zhang, Y. Yang and Y. Tang, UV-to-IR highly transparent ultrathin diamond nanofilms with intriguing performances: Anti-fogging, self-cleaning and self-lubricating, *Appl. Surf. Sci.*, 2020, **527**, 146733.
- 15 J. Millán-Barba, M. Gutiérrez, F. Lloret, R. G. de Villoria, R. Alcántara, K. Haenen and D. Araujo, Study of early stages in the growth of boron-doped diamond on carbon fibers, *Phys. Status Solidi A*, 2021, **218**(5), 2000284.



- 16 S. S. Nicley, S. Drijkoningen, P. Pobedinskas, J. Raymakers, W. Maes and K. Haenen, Growth of boron-doped diamond films on gold-coated substrates with and without gold nanoparticle formation, *Cryst. Growth Des.*, 2019, **19**(6), 3567–3575.
- 17 J. Delchevalrie, S. Saada, R. Bachelet, G. Saint-Girons and J. C. Arnault, Spectroscopic ellipsometry: A sensitive tool to monitor domains formation during the bias enhanced nucleation of heteroepitaxial diamond, *Diamond Relat. Mater.*, 2021, **112**, 108246.
- 18 G. Cicala, V. Magaletti, G. S. Senesi and M. Tamborra, Smoothness improvement of micrometer- and submicrometer-thick nanocrystalline diamond films produced by MWPECVD, *J. Nanopart. Res.*, 2013, **15**(4), 1549.
- 19 M. Schreck, J. Asmussen, S. Shikata, J. C. Arnault and N. Fujimori, Large-area high-quality single crystal diamond, *MRS Bull.*, 2014, **39**, 504–510.
- 20 S.-W. Kim, Y. Kawamata, R. Takaya, K. Koyama and M. Kasu, Growth of high-quality one-inch free-standing heteroepitaxial (001) diamond on (11 2 0) sapphire substrate, *Appl. Phys. Lett.*, 2020, **117**(20), 202102.
- 21 R. C. M. de Barros, E. J. Corat, N. G. Ferreira, T. M. de Souza, V. J. Trava-Airoldi, N. F. Leite and K. Iha, Dispersion liquid properties for efficient seeding in CVD diamond nucleation enhancement, *Diamond Relat. Mater.*, 1996, **5**(11), 1323–1332.
- 22 C. Norgard, K. Glejbol, S. S. Eskildsen and A. Matthews, Enhanced diamond nucleation density utilising seeding, *Diamond Relat. Mater.*, 1998, **7**, 1278–1281.
- 23 R. Akhvediani, I. Lior, S. Michaelson and A. Hoffman, Nanometer rough, sub-micrometer-thick and continuous diamond chemical vapor deposition film promoted by a synergetic ultrasonic effect, *Diamond Relat. Mater.*, 2002, **11**(3), 545–549. 12th European Conference on Diamond, Diamond-Like Materials, Carbon Nanotubes, Nitrides & Silicon Carbide.
- 24 S. Mandal, K. Arts, H. C. M. Knoops, J. A. Cuenca, G. M. Klemencic and O. A. Williams, Surface zeta potential and diamond growth on gallium oxide single crystal, *Carbon*, 2021, **181**, 79–86.
- 25 E. J. W. Smith, A. H. Piracha, D. Field, J. W. Pomeroy, G. R. Mackenzie, Z. Abdallah, F. C. P. Massabuau, A. M. Hinz, D. J. Wallis, R. A. Oliver, M. Kuball and P. W. May, Mixed-size diamond seeding for low-thermal-barrier growth of CVD diamond onto GaN and AlN, *Carbon*, 2020, **167**, 620–626.
- 26 K. H. Lee, W. K. Seong and R. S. Ruoff, CVD diamond growth: Replacing the hot metallic filament with a hot graphite plate, *Carbon*, 2022, **187**, 396–403.
- 27 D. Banerjee, K. J. Sankaran, S. Deshmukh, M. Ficek, C. J. Yeh, J. Ryl, I. N. Lin, R. Bogdanowicz, A. Kanjilal, K. Haenen and S. Sinha-Roy, Single-step grown boron doped nanocrystalline diamond-carbon nanograss hybrid as an efficient supercapacitor electrode, *Nanoscale*, 2020, **12**, 10117–10126.
- 28 S. Mandal, H. A. Bland, J. A. Cuenca, M. Snowball and O. A. Williams, Superconducting boron doped nanocrystalline diamond on boron nitride ceramics, *Nanoscale*, 2019, **11**, 10266–10272.
- 29 E. Scorsone, S. Saada, J. C. Arnault and P. Bergonzo, Enhanced control of diamond nanoparticle seeding using a polymer matrix, *J. Appl. Phys.*, 2009, **106**(1), 014908.
- 30 M. Tsigkourakos, T. Hantschel, S. D. Janssens, K. Haenen and W. Vandervorst, Spin-seeding approach for diamond growth on large area silicon-wafer substrates, *Phys. Status Solidi A*, 2012, **209**(9), 1659–1663.
- 31 O. Shenderova, S. Hens and G. McGuire, Seeding slurries based on detonation nanodiamond in DMSO, *Diamond Relat. Mater.*, 2010, **19**(2), 260–267. NDNC 2009.
- 32 S. Mandal, C. Yuan, F. Massabuau, J. W. Pomeroy, J. Cuenca, H. Bland, E. Thomas, D. Wallis, T. Batten, D. Morgan, R. Oliver, M. Kuball and O. A. Williams, Thick, adherent diamond films on AlN with low thermal barrier resistance, *ACS Appl. Mater. Interfaces*, 2019, **11**(43), 40826–40834.
- 33 M. Tsigkourakos, T. Hantschel, D. K. Simon, T. Nuytten, A. S. Verhulst, B. Douhard and W. Vandervorst, On the local conductivity of individual diamond seeds and their impact on the interfacial resistance of boron-doped diamond films, *Carbon*, 2014, **79**, 103–112.
- 34 S. D. Janssens, D. Vázquez-Cortés and E. Fried, Formation and morphology of closed and porous films grown from grains seeded on substrates: two-dimensional simulations, *Acta Mater.*, 2022, **225**, 117555.
- 35 H. Aida, R. Oshima, T. Ouchi, Y. Kimura and A. Sawabe, In-situ reflectance interferometry of heteroepitaxial diamond growth, *Diamond Relat. Mater.*, 2021, **113**, 108253.
- 36 C. Delfaure, N. Tranchant, J.-P. Mazellier, P. Ponard and S. Saada, Monitoring texture formation during diamond growth by specular and diffuse reflectance interferometry, *Diamond Relat. Mater.*, 2016, **69**, 214–220.
- 37 G. Chen, L. Spentzouris, K. K. Kovi and S. V. Baryshev, Submicrometer ultrananocrystalline diamond films processed in oxygen and hydrogen plasma and analyzed by UV-vis spectroscopy: thickness and optical constant results, *Surf. Sci. Spectra*, 2020, **27**(2), 026601.
- 38 C. Wu, W. H. Weber, T. J. Potter and M. A. Tamor, Laser reflective interferometry for in situ monitoring of diamond film growth by chemical vapor deposition, *J. Appl. Phys.*, 1993, **73**(6), 2977–2982.
- 39 C. D. Zuiker, D. M. Gruen and A. R. Krauss, In situ laser reflectance interferometry measurement of diamond film growth, *J. Appl. Phys.*, 1996, **79**(7), 3541–3547.
- 40 A. M. Bonnot, B. S. Mathis and S. Moulin, Investigation of the growth kinetics of low pressure diamond films by in situ elastic scattering of light and reflectivity, *Appl. Phys. Lett.*, 1993, **63**(13), 1754–1756.
- 41 A. A. Smolin, V. G. Ralchenko, S. M. Pimenov, T. V. Kononenko and E. N. Loubnin, Optical monitoring of nucleation and growth of diamond films, *Appl. Phys. Lett.*, 1993, **62**(26), 3449–3451.
- 42 A. J. Cox, A. J. DeWeerd and J. Linden, An experiment to measure Mie and Rayleigh total scattering cross sections, *Am. J. Phys.*, 2002, **70**(6), 620–625.



- 43 P. Pobedinskas, G. Degutis, W. Dexters, J. D'Haen, M. K. Van Bael and K. Haenen, Nanodiamond seeding on plasma-treated tantalum thin films and the role of surface contamination, *Appl. Surf. Sci.*, 2021, **538**, 148016.
- 44 P. Klapetek, I. Ohlidal, A. Montaigne-Ramil, A. Bonanni, D. Stifter and H. Sitter, Atomic force microscopy characterization of ZnTe epitaxial thin films, *Jpn. J. Appl. Phys.*, 2003, **42**(part 1, no. 7B), 4706–4709.
- 45 S. J. Orfanidis, *Electromagnetic Waves and Antennas*, Ch.~8, Multilayer film applications, <https://www.ece.rutgers.edu/~orfanidi/ewa/ch08.pdf>, accessed November 2022.
- 46 N. O. Mchedlov-Petrosyan, N. N. Kamneva, A. I. Marynin, A. P. Kryshtal and E. Osawa, Colloidal properties and behaviors of 3 nm primary particles of detonation nanodiamonds in aqueous media, *Phys. Chem. Chem. Phys.*, 2015, **17**(24), 16186–16203.
- 47 J. C. Arnault, S. Saada, M. Nesladek, O. A. Williams, K. Haenen, P. Bergonzo and E. Osawa, Diamond nanoseeding on silicon: stability under H₂ MPCVD exposures and early stages of growth, *Diamond Relat. Mater.*, 2008, **17**(7), 1143–1149. Proceedings of Diamond 2007, the 18th European Conference on Diamond, Diamond-Like Materials, Carbon Nanotubes, Nitrides and Silicon Carbide.
- 48 A. V. Stanishevsky, M. J. Walock and S. A. Catledge, Surface modification and stability of detonation nanodiamonds in microwave gas discharge plasma, *Appl. Surf. Sci.*, 2015, **357**, 1403–1409.
- 49 W. G. S. Leigh, E. L. H. Thomas, J. A. Cuenca, S. Mandal and O. A. Williams, In situ monitoring of microwave plasma-enhanced chemical vapour deposition diamond growth on silicon using spectroscopic ellipsometry, *Carbon*, 2023, **202**, 204–212.
- 50 A. Van der Drift, A principle governing growth orientation in vapour-deposited layers, *Philips Res. Rep.*, 1967, **22**, 267–288.

